Electronic Polarizability Tunes the Function of the Human Bestrophin 1 Cl^- Channel

Linda X. Phan[1,2], Aaron P. Owji[3,4,5], Tingting Yang[3], Jason Crain[2,6], Mark S.P. Sansom[2], and Stephen J. Tucker[1,7]*

[1] Clarendon Laboratory, Department of Physics, University of Oxford, Oxford, OX1 3PU, UK

[2] Department of Biochemistry, University of Oxford, Oxford, OX1 3QU, UK

[3] Department of Opthalmology, Columbia University, New York, NY, USA

[4] Department of Pharmacology, Columbia University, New York, NY, USA

[5] Simons Electron Microscopy Center, New York Structural Biology Center, New York, NY 10027, USA

[6] IBM Research Europe, Hartree Centre, Daresbury, WA4 4AD, UK

[7] Kavli Institute for Nanoscience Discovery, University of Oxford, OX1 3QU, UK

* To whom correspondence should be addressed:

stephen.tucker@physics.ox.ac.uk

Keywords
Molecular dynamics, anion permeation, chloride selectivity, anion-π, Bestrophin channels

Abstract

Mechanisms of anion permeation within ion channels and nanopores remain poorly understood. Recent cryo-electron microscopy structures of the human bestrophin 1 chloride channel (hBest1) provide an opportunity to evaluate ion interactions predicted by molecular dynamics (MD) simulations against experimental observations. We implement the fully polarizable forcefield AMOEBA in MD simulations of open and partially-open states of the hBest1. The AMOEBA forcefield models multipole moments up to the quadrupole; therefore, it captures induced dipole and anion-π interactions. By including polarization we demonstrate the key role that aromatic residues play in ion permeation and the functional advantages of pore asymmetry within the highly conserved hydrophobic neck of the pore. We establish that these only arise when electronic polarization is included in the molecular models. We also show that Cl^- permeation in this region can be achieved through hydrophobic solvation concomitant with partial ion dehydration, which is compensated for by the formation of contacts with the edge of the phenylalanine ring. Furthermore, we demonstrate how polarizable simulations can help determine the identity of ion-like densities within high-resolution cryo-EM structures. Crucially, neglecting polarization in simulation of these systems results in the localization of Cl^- at positions that do not correspond with their experimentally resolved location. Overall, our results demonstrate the importance of including electronic polarization in realistic and physically accurate models of biological systems.

Statement of Significance

Ion channels are nanoscale protein pores that enable the selective passage of charged ions across cell membranes. Understanding the underlying mechanisms for selective anion permeation through such pores remains a challenge. To simulate their behavior efficiently *in silico*, fixed charge models are typically employed. However, this approach is insufficient for the study of anions. Here, we use simulations with explicit treatment of electrostatics to investigate the interactions of chloride ions in the human bestrophin 1 channel. We find that electronic polarization tunes the state of the channel and affects the interactions of chloride ions thereby revealing a mechanism for permeation. Furthermore, these simulations can be used to resolve experimental ambiguity in ion-like densities from cryo-EM structures.

Introduction

Ion channels are nanoscale pore-forming membrane proteins that enable the rapid and selective passage of ions across a membrane. Their activity and function are central to the regulation of physiological processes from cell signaling and the control of pH balance, to muscle contraction and brain function (1, 2). Chloride ions are the most abundant anion in living organisms. Since dysfunction of associated Cl^- channels is known to result in a variety of disease states, these proteins represent attractive therapeutic targets (3). However, the underlying mechanisms of Cl^- permeation and selectivity in these channels remain under-explored relative to their cation counterparts, and is partly a consequence of their weak selectivity (4). It is therefore of great interest to explore the mechanisms of anion permeation in such channels and to thoroughly assess the essential physics needed for accurate functional annotation.

Studies suggest that Cl^- can form favorable interactions with hydrophobic interfaces ranging from simple air/water interfaces to more complex protein interfaces (5–7). The anisotropy of such interfaces induces a dipole in the Cl^- that is otherwise not present in bulk. Interactions between the induced dipole and surrounding water molecules compensate for the partial dehydration of Cl^- as it adsorbs at the interfacial layer and comes into direct contact with the hydrophobic interface (8). This phenomenon can be observed across the Hofmeister series i.e., $F^- < Cl^- < Br^- < I^-$, whereby the softer, more polarizable anions are more prone to dehydration and localize at the interface (9).

Anion interactions with aromatic edges are also a well-established phenomenon (10–12) and more recently been recognized to play important roles in buried regions of proteins (11, 13). Also, the ion conduction pathway within some anion channels can be composed of aromatic residues such as phenylalanine. Known structures of anion channels that exploit this include the mechanosensitive Cl^- channel, Flycatcher1 (FLYC1) where the narrowest constriction (~ 2.8 Å radius) is created by a ring of phenylalanine side chains (14), the slow anion channel (SLAC1) which is occluded by a highly conserved phenylalanine residue responsible for channel gating (< 2 Å) (15) and the mechanosensitive channel of small conductance from *Escherichia coli* (EcMscS) in which phenylalanines appear to constitute the hydrophobic gate (~ 4 Å) (16). However, although such anion-aromatic interactions are readily observed, the degree to which dilation is required for anion passage in the presence of pore-ling phenylalanine residues is variable and only partially understood. Therefore, there is a need for further biophysical characterization to better understand the functional roles of such pore-lining aromatics and their contributions towards anion permeation.

Cryo-electron microscopy (cryo-EM) is a powerful structural technique that has revolutionized the field of structural biology. Recent technological improvements in sample treatment, grid preparation, microscope hardware, and image processing have made it achievable to obtain high-resolution maps better than 3 Å (17). Despite these advancements, there are several caveats, such as radiation damage, resulting in lower signal-to-noise ratios, protein denaturation and beam-induced sample movement, which all present limitations to achieving even higher resolutions (18). The resolution of single-particle cryo-EM is also often insufficient to provide detailed information on small molecules or bound ligands, such as water or ions, which require a resolution of at least 2.5 Å (19), and so it can be difficult to differentiate and interpret these small densities with confidence when using this technique. Molecular dynamics (MD) simulations can extend the capabilities of cryo-EM by capturing conformational variability and short-lived states. Furthermore, MD simulations can assist in

the assignment and interpretation of cryo-EM data to access improved atomic resolution structures (20).

The majority of MD simulations employ pairwise additive forcefields that model electrostatic interactions as Coulombic forces between fixed point charges (21). These forcefields do not capture the effects of induced polarization that arise from redistributions of charge density in response to local field gradients. This becomes problematic for modelling systems that involve polarizable moieties, such as aromatic residues and polarizable anions. A number of biomolecular forcefields have recently been developed to capture induced polarization. Among these, two of the most widely employed are the AMOEBA forcefield (22) which models atomic monopoles through to quadrupole moments within a classical MD framework, and the CHARMM Drude forcefield (23, 24), which uses massless Drude oscillators to displace charge from atomic centers. These forcefields provide new and improved levels of predictive power over non-polarizable forcefields; however, they incur additional computational costs. It is therefore important to identify situations where such capability can add value and provide new biological insights.

An example where modelling polarization may be vital is in the study of Cl^--selective ion channels. Due to the weakly polarizable nature of Cl^- (25), realistic behavior is subtle and often difficult to capture. A suitable model are the Bestrophin channels, a family of calcium-activated Cl^- channels (CaCCs) where many questions still remain (26, 27). Four paralogs (Best1-4) have been identified in eukaryotes which are responsible for a diverse range of functions (27). The best-known physiological role of Best1 is in the eye where disease-causing mutations cause retinal degenerative disorders called bestrophinopathies. The structures of bestrophin channels contain two key constrictions in the ion conduction pathway. A permeating ion from the extracellular side will first encounter the neck region, which is a gate composed of three hydrophobic residues (I76, F80 and F84) that are highly conserved across homologs. After passing this gate, the ion will traverse the interior of the cytosolic vestibule, followed by a second, shorter constriction at the cytosolic exit, called the aperture, which displays significant divergence across paralogs (27), but together, the neck and aperture are both thought to comprise part of the gating mechanism for bestrophin channels, although their relative contribution to gating and/or Cl^- selectivity remain unclear (27–30).

Comparison of the human Bestrophin 1 channel (hBest1) in the fully open state (PDB ID 8D1O, 2.4 Å resolution) (**Fig. 1A-C, G**) with the partially open neck state (PDB ID 8D1K, 2.3 Å resolution) (**Fig. 1D-G**) (29) reveals a conformational change in the pore-facing residues of the hydrophobic neck (**Fig. 1B & 1E).** This difference allow us to probe the mechanisms of ion permeation and selectivity, as well as the conformational pathway to channel opening.

In this study, we therefore explore the effect of electronic polarization on hBest1 function by implementing fully polarizable forcefields to examine the behavior of Cl- within the neck region. Here, we present an example of how such forcefields provide novel detailed insights into channel function and the behavior of Cl^- in the neck of hBest1. They also reveal the roles of aromaticity and pore asymmetry in ion permeation. In particular, phenylalanine sidechains are seen to undergo a conformational change which enables edge-on interactions with a partially-dehydrated Cl^- during permeation. Crucially, we also show that models which include realistic polarization can be used to interpret ambiguous ion-like densities observed in

experimental high-resolution cryo-EM structures, thus enabling more accurate functional annotation.

Results & Discussion

To probe the role of the conserved neck region in bestrophin channels, we have performed atomistic MD simulations of fragments from hBest1 containing the neck region and pore-lining sections from both the fully open (PDB ID 8D1O) and partially-open neck states (PDB ID 8D1K). These fragments consisted of residues 56 to 99 from the full protein and were simulated in a 0.5 M NaCl solution (**Fig. S1**). Previous studies of reduced systems of ion channels focusing on isolated sections have shown that they can provide an accurate representation of the dynamics within the original protein (6, 31, 32). To validate the protein fragment, we performed simulations of the full protein embedded in a lipid bilayer compared with the protein fragment and analyzed the average water density. The resulting profiles are similar, and the average water density remains close to bulk outside the neck region (**Fig. S2**). This provides confidence that the protein fragments in our reduced system offer a representative model of the fully open and hydrated pore from the full protein.

The system contains aromatic residues and polarizable ions and therefore justifies the use of fully polarizable forcefields, such as AMOEBA. However, with added complexity comes increased computational costs, hence the need to reduce the system size to make the simulations computationally feasible.

Interpretation of cryo-EM densities from fully polarizable MD simulations

In the experimental structure of the open state hBest1, a number of non-protein, ion-like densities have been observed, which have been modelled as water molecules in the published structure. A set of these water molecules (corresponding to HOH739 and HOH539 in the PDB) are located within the neck region and appear to bind to the helix dipole (33) at a distance of 3.2 Å to the backbone NH of F80 of each chain (**Fig. 2A**). Similar non-protein densities are also observed consistently in proximity to the helix dipole in the open state structure of human bestrophin 2 (hBest2) (PDB ID 8D1N). Due to experimental limitations, there is ambiguity in the molecular identity of these densities. Assessment of the local chemistry and comparisons with known bromide binding sites from anomalous scattering studies of a Best1 homolog (34) suggest the location of these densities are comparable to the putative water molecules in the hBest1 structure. Therefore, it has been suggested that this site could possibly serve as a Cl^- binding site. Here, we have used the AMOEBA forcefield to explore the possibility that these densities could instead be representative of Cl^-. We refer to the density X739 as the ion-like density previously labelled as a water molecule (HOH739) in the PDB.

Analysis of the z-positions of ions and water as a function of time revealed that the open state neck is wetted and permeable to ions. There is a clear accumulation of Cl^- in the region between I76 and F80 of the neck (indicated by the dense orange region in **Fig. 2B**). An electric double layer also forms and sodium ions are largely excluded from regions below I76 (**Fig. 2B**). To pinpoint precisely where Cl^- is clustering in three dimensions, we have used the computational tool, PyLipID, which is capable of analyzing protein-ligand interactions (35). Taking the top-ranked binding pose for the detected binding site, we focus on interactions of a single chain and have aligned the simulated fragment structures with the original PDB structure (chain E and HOH739) for comparison (**Fig. 2C**).

The results of the AMOEBA simulations correlate very well with the cryo-EM densities. A number of identified binding sites in the neck region are within 1.5 Å of the ion-like density (**Fig. S3**) and we show the binding site that is most representative of the density associated with HOH739 in the original structure (**Fig. 2C-E**). A significant overlap can be seen between the Cl^- and the water molecule modelled in the PDB structure (**Fig. 2D**). The distance of the Cl^- to the backbone nitrogen of F80 is 3.8 Å compared with 3.2 Å in the experimental structure (**Fig. 2E**) and it is equidistant from the pore axis. Studies of CLC channels have revealed that pore-lining backbone amides can influence ion selectivity and permeation (4). Therefore, it is feasible that the ion-like density in this experimental structure is not water but a Cl^-. This difference in ion location between the simulation and structural densities could be a result of the imposition of 5-fold symmetry during structural processing, which could marginally shift the cryo-EM density in comparison to allowed asymmetric interaction modes. Conversely, from a simulation perspective, the localization of Cl^- can be forcefield dependent and conditional on the realism of the model.

To demonstrate the impact of modelling polarizability, equivalent simulations were also performed with the non-polarizable forcefield, CHARMM36m (c36m) (**Fig. 2F**). In contrast to the AMOEBA simulations, these simulations suggest that Cl^- tends to localize at a distance of 5.1 Å from the backbone nitrogen of F80 (**Fig. 2H**) and prefers to interact with the backbone NH, hydroxyl group of S79, and the backbone NH of I78 (**Fig. 2G**). The c36m simulations do not detect the same Cl^- binding geometries as the ones yielded by the AMOEBA simulations and experimental density. Furthermore, no alternative binding conformations within the neck region are detected for c36m simulations.

Functional advantages of pore asymmetry

It is common practice in cryo-EM to apply rotational symmetry in the map construction and refinement process. Regions of structure that present heterogeneous features are averaged over several images. Averaging leads to the loss of information of individual differences between protomers. It is possible to extract heterogeneous regions through methods such as the application of 3D masks during classification and refinement (17, 36). However, applying a small mask to putative ions or water molecules is difficult due to the size of the features and may be unsuccessful in providing any additional structural information.

MD simulations enable examination of the functional role that asymmetry may plays in the neck which would otherwise not be easily deduced from experimental structures. In the open state structure, the sidechains of F80 and F84 are pore-facing whilst the side chain of I76 turns away from the ion-conducting pore. The pore radius in the neck region is sufficiently large to accommodate a fully hydrated Cl^- (radius ~ 4 Å (37)) and from **Fig. 2B**, the pore is wetted and permeable to ions in the neck. Therefore, it is of interest to study how these ions are coordinated, their permeation mechanisms and whether pore asymmetry presents any functional advantages in this neck region.

Throughout the AMOEBA forcefield simulation, asymmetric states of the pore at F80 can be observed. The sidechains of F80 exhibit two discrete conformations illustrated in the RMSD of F80 per chain of the protein (**Fig. S4**) with dynamical pathways between them. To dissect the dynamics of the side chains, we characterized the motions into three components: firstly, the torsion angle, χ_2 (CA-CB-CG-CD1) which captures the orientation of the aromatic ring (**Fig. 3A**). Secondly, the angle θ between vectors defined by F80 CA and F84 CA of the same chain and F80 CA with the carbon atom, CZ from the aromatic ring, defines the vertical

up/down motion of the F80 sidechain in the z-direction (**Fig. 3B**). Finally, the distance *xy* defines the distance between atom CZ of F80 from one chain (N) and the CA atom from F80 in the neighboring chain (N+1), which characterizes the F80 sidechain conformation as facing inward towards the pore axis or outwards as found in the experimental structure (**Fig. 3C**).

In the fully open state, the sidechains of F80 are oriented in an outwards conformation relative to the pore axis. Here, we focus on the dynamics of a single chain (chain 5). At time t ~ 10 ns, the sidechain simultaneously moves in a vertical upwards direction (θ) whilst flipping inwards towards the pore (*xy*) and rotating the aromatic ring from a flat orientation to a vertical upright position (χ_2) (**Fig. 3D**). For the duration of the vertical ring-oriented conformation, a nearby Cl^- may then form edgewise anion-π interactions with the ring (discussed below). We observe that these Cl^--π interactions are transient. After ~ 25 ns, the sidechain spontaneously reorients back to the outwards-flipped conformation. Although the presence of a Cl^- does not necessarily induce the inward/outward flipping of F80 (**Fig. S5**), the flipped sidechain may be functionally advantageous for ion permeation. However, there is no clear correlation between the motion of these sidechains and interactions with Cl^- in the immediate vicinity; at times, flipping occurs concurrently in the presence of a Cl^-, and at other times, it occurs spontaneously. This dynamic behavior is reversible and is observed across multiple chains (**Fig. S4**). It is also suggestive of more conformational diversity than is captured in the symmetrized cryo-EM structure.

The role of water in Cl^- permeation

Despite the dimensions of the open neck being wide enough to accommodate a hydrated Cl^-, we observe that permeation through the neck can be associated with the stripping of 1-3 water molecules from the first hydration shell of the ion (**Fig. 3E**). The dynamic inward ring flipping behavior of F80 can aid the permeation of ions; the loss of a single water molecule from the first hydration shell of Cl^- is compensated by an interaction with the benzene ring from a single F80 sidechain and, similarly, the loss of more than one water molecule correlates to interaction with two inwards-flipped sidechains from adjacent protomers (38, 39) (**Fig. 3F**). A maximum of two inwards-flipped sidechains can be observed in a single instance and always occur between two adjacent protomers.

The removal of water molecules allows for direct contact between Cl^- and the hydrophobic aromatic rings mediated through anion-π interactions. The benzene ring of the phenylalanine has a large negative quadrupole moment that creates a partial negative charge on both faces of the π-system and subsequently a partial positive charge around the edge of the ring (12, 40, 41). As a result, the partial loss of solvation of Cl^- can be compensated by favorable interactions with these aromatic rings which could be regarded as “hydrophobic solvation”. It has been hypothesized (28–30, 34) that such a mechanism may mediate the stabilization of a dehydrated Cl^- at F80 and F84 through anion-π interactions based on the initial X-ray structure of chicken Best1 (cBest1), although this structure was later determined to be in the closed conformation. Mutagenesis studies of the cBest1 neck residues to alanine later showed no effect on ion selectivity and suggested that the role of anion-π interactions may reduce the energy barriers for Cl^- and other anions to permeate the neck region but not be the determining factor for charge selectivity (42, 43). Other forms of hydrophobic solvation mechanisms have previously been observed in simulations of a biomimetic nanopore (44) and

a hydrophobic protein binding site (32) whereby Cl^- moved through pores by partially dehydrating and forming energetically favorable interactions with hydrophobic contacts.

These anion-hydrophobic interactions were only observed when electronic polarization was included in the molecular model and are not observed in equivalent simulations of the open state hBest1 when using fixed-charge (c36m) descriptions. We attribute this to the fact that anion-π interactions arise mainly from two factors: electrostatic interactions of the quadrupole moment and ion-induced polarization (41); the latter of which is not captured in c36m (45). This is clearly reflected in the single chain RMSDs for c36m (see **Fig. S6**)

Pathway for conformational change between open and partially open states

Simulations of the open state hint at a possible conformational transition pathway between the open and partially open states. The conformation of the inwards-flipped F80 sidechains in the open state resemble the conformation of F80 in the partially open state. In the partially open state, the F80 sidechains remain stable in an inward facing arrangement throughout the simulation with $\chi_2 \sim 275°$, a torsion angle between that of the open state fluctuations (flat ~ 255°, vertical ~ 285°). In the partially open state, the angle $\theta \sim 140°$ is approximately the same as the position of F80 in the inwards-flipped state of the open neck which suggests the sidechain moves via an elevated vertical position towards a more closed state (**Fig. S7**). These fluctuations in F80 sidechains in the open state mimic the structure of the partially open state, therefore it suggests a potential mechanism for transitioning of the neck residues from an open, conductive state to a partially open state and vice versa.

Analysis of the partially open neck state

The partially open structure of hBest1 presents a more constricted neck region (**Fig. 1E**). Critical conformational changes occur in residues F282, F283, and F276 concomitant with changes in neck residues I76, F80 and F84. I76 remains facing away from the pore axis as in the fully open state, while residues F80 and F84 and the hydrophobic gating apparatus adopt a closed-like conformation (**Fig. 1G**) (29). In the experimental structure, an ion-like density is consistently captured at the edge of F84, even when processed with C1 refinement (Fig. S1 D from (29)) i.e., with no symmetry applied. This density could potentially represent a chemical constituent of the buffer system, in which Cl^- is the predominant ion, and so may represent a dehydrated Cl^-. Furthermore, asymmetry in the neck can be observed as continuous movement between the closed and intermediate states in this region.

Trajectories of ions and water in the partially-open state protein fragment (**Fig. 4A**) see traces of Cl^- occupying locations just above F84 in the z-direction. This suggests that F84 is capable of accommodating Cl^-; however, the pore is functionally closed as ions are not conducted across the neck, primarily due to the tight constriction formed by F80. Additionally, a small, transiently dewetted region can be found within the neck (represented by the white band), corresponding to residues S79 and F80, which reiterates that the partially open state is functionally closed (**Fig. 4A**). This is more clearly depicted in **Fig. 4C & 4D,** where the orange mesh describes the volume of space that Cl^- occupies throughout the simulation. The majority of the neck region is devoid of Cl^-, as indicted by the dewetted region, since pore hydration acts as a precursor to ion permeation (**Fig. 4D**). Mutagenesis studies have demonstrated that the conserved "IFF" motif of the neck acts as an effective gate, rather than a selectivity filter, because ionic selectivity remained constant in the mutant channel (42, 46) which is in agreement with our results.

F84 accommodates for a Cl^- through a similar mechanism to that seen in the previous section: the Cl^- partially dehydrates (**Fig. S8**) to directly interact with up to 2 adjacent pore-facing phenylalanines simultaneously, mediated by their edge-wise interaction with the

partially dehydrated anion (**Fig. 4E**). The sidechains of F84 remain stable in their inward-facing conformation throughout the simulations as determined by the low RMSD. This two-state behavior largely corresponds to a 180° reorientation of the aromatic ring (**Fig. S9**).

Together, these observations support functional annotation of the channel as "partially open." It is indeed "on-the-way" to opening/closing with the neck containing a consistently dewetted region and presenting a barrier to ion permeation, yet the neck (F84) can accommodate Cl^-. This barrier to ion permeation is not necessarily due to steric occlusion, but rather to the inability of the Cl^- to shed more of the first hydration shell. The partially open neck is wide enough to accommodate a dehydrated Cl^- (**Fig. 4A & 4B**) but it is energetically unfavorable to lose more than ~ 2-3 water molecules in the neck region at the tightest constriction which would be required for permeation and therefore ions do not pass through this region.

For comparison, in the absence of polarization, c36m simulations suggest the neck is functionally closed and there is a more prominent dewetted region at S79 and F80. F84 does not accommodate Cl^- but water can occupy this region (**Fig. 4B**).

Conclusions

We have performed MD simulations of the neck region of hBest1 channels in the open and partially open neck states using a fully polarizable forcefield (AMOEBA). Our results demonstrate that electronic polarization plays a key role in Cl^- accumulation at the helix dipole (the backbone nitrogen of F80) in the open state with significant overlap with an ion-like density previously assigned to a water molecule in the cryo-EM structure. Together, our data suggest that this location functions as a Cl^- binding site that contributes to anion selectivity in the open neck conformation of bestrophins. In contrast, fixed charge (c36m) simulations predict a different location for Cl^- accumulation that is not supported by experimental data, thus underscoring the importance of forcefield choice in simulation-based functional annotation of polarizable systems. Cl^- permeation through the open neck region is facilitated by edgewise anion-π interactions with the aromatic sidechains of F80 where, again, the influence of electronic polarization appears to exert decisive influence over the functional state of the channel. These sidechains dynamically and reversibly flip inwards towards the pore axis to interact directly with a partially dehydrated Cl^-. Simulations of the partially open neck state also support this permeation mechanism as neck dilation at F84 is able to accommodate Cl^-; however, the pore remains functionally closed and is therefore 'partially' open. Conversely, c36m simulations predict this partially open state structure to be closed. This study therefore provides new insights into bestrophin channel function although further studies are required to separate the individual contributions of structural elements to Cl^- permeation and selectivity within the ion pathway.

Overall our results demonstrate the importance of modelling polarization in situations where polarizable moieties play an essential role in protein function. Appropriate treatment of electrostatics reveals more physically accurate behavior and provides new mechanistic insights into Cl^- permeation. MD simulations employing explicit polarization can therefore complement cryo-EM and other structural techniques in the identification and assignment of ambiguous non-protein densities such as anions.

Methods

Structural model and system preparation

Cryo-EM structures of human Bestrophin 1 (hBest1) in the Ca^{2+}–bound open state (PDB ID 8D1O, 2.4 Å resolution) and the hBest1 Ca^{2+}–bound partially open neck state (PDB ID 8D1K, 2.3 Å resolution) (29) obtained from the Protein Data Bank (PDB). Due to the methodological and high computational demands for implementing explicitly polarizable forcefields, we reduced the protein structures to include the pore-lining segments spanning most of the transmembrane domain. The protein fragments were composed of residues 56 to 99, which encompass the neck region of interest (residues I76, F80 and F84) (**Fig. S1**). Protein fragment systems were solvated in a 0.5 M NaCl solution and were prepared using the CHARMM-GUI protocol (47).

Non-polarizable molecular dynamics

MD simulations employing a non-polarizable forcefield were performed in GROMACS (48) version 2021 using the CHARMM36m (c36m) forcefield in conjunction with the mTIP3P water model. Protein fragment systems were first subjected to energy minimization followed by a 2 ns NVT equilibration period. Simulations in the NPT ensemble were conducted for 100 ns whereby the first 20 ns of each simulation were discarded as an equilibration. Therefore, the final 80 ns of the simulation were used for analysis.

Simulations were carried out using the leap-frog integrator with a timestep of 2 fs. The temperature was maintained at 310 K using the Nosé-Hoover thermostat (49) with a time coupling constant of 1.0 ps. The pressure was maintained at 1 bar using the Parrinello-Rahman barostat (50) with a time coupling of 5.0 ps. Short-range electrostatics were treated with the Verlet cutoff scheme with a cutoff at 1.2 nm and long-range electrostatics were treated with the particle mesh Ewald (PME) algorithm (51). The LINCS algorithm (52) was used to constrain h-bonds. Backbone atoms were placed under harmonic restraints with a force constant of 1000 kJ/mol/nm^2 to prevent the structures from deviating too much from the experimental coordinates. Three independent repeats were carried out for each system.

Polarizable simulations molecular dynamics

Fully polarizable forcefield simulations were carried out in OpenMM 7.4.2 (www.openmm.org) and all components in the system were modelled with the AMOEBA polarizable forcefield using the amoeba2018 parameter set (53, 54). Starting configurations for these simulations were obtained from the end of the NVT ensemble equilibration period using c36m as described above. Simulations were then setup following a similar procedure to a method described previously (https://github.com/Inniag/openmm-scripts-amoeba) (6).

AMOEBA forcefield simulations proceeded by performing 1000 steps of energy minimization to resolve any divergent energies due to the induced dipoles. The production run was simulated for 60 ns, with the first 10 ns of the simulation discarded for equilibration; therefore, the final 50 ns were used for analysis. Time integration was performed using the r-RESPA multiple time step integration algorithm (55) with an inner time step of 0.25 fs and an outer time step of 2 fs. The temperature was maintained at 310 K using the Andersen thermostat and pressure was maintained at 1 bar using the isotropic Monte Carlo barostat. Electrostatic multipole interactions were evaluated by the PME method with a real-space cutoff of 8 Å and tolerance of 5×10^{-4} and a fifth order B-spline interpolation. VdW interactions were calculated explicitly up to a distance of 12 Å and interactions beyond this cutoff treated with an analytical long-range dispersion correction. All C_α atoms were placed under a harmonic restraint with force constant 1000 kJ/mol/nm^2 to prevent the protein from deviating from the experimental structure.

Binding site identification and analysis

Interactions of Cl^- with each protein structure, binding site detection and quantification were calculated using PylipID (https://github.com/wlsong/PyLipID) (35). Binding sites were defined by Cl^- contact with three or more residues and by a dual-cutoff scheme for which Cl^- were considered bound if they resided between 3.3 Å and 4.8 Å based on data from the first hydration shell of Cl^- using the amoeba forcefield. Alignment and visualization of structures were achieved using Pymol (https://pymol.org/2/). Trajectory analysis was performed using MDAnalysis (56, 57) and GROMACS analysis tools (58). The pore radius profiles were obtained using CHAP (www.channotation.org) (59).

Acknowledgements

We thank T. Bertie Ansell for their insightful discussions regarding analysis and usage of PylipID. We would like to acknowledge the ARCHER2 UK National Supercomputing Service (http://www.archer2.ac.uk) and the University of Oxford Advanced Research Computing (ARC) facility in carrying out this work (http://dx.doi.org/10.5281/zenodo.22558). This work was supported by grants from the Biotechnology and Biological Sciences Research Council, the Engineering and Physical Sciences Research Council and National Institutes of Health grant R35GM149252.

Author contributions

All authors designed research and wrote the paper. L.X.P performed research and analyzed data. S.J.T, J.C, M.S.P.S and T.Y obtained funding for the project.

Declaration of interests

J.C. is an employee of IBM Research.

Figure Legends

Figure 1: Cryo-EM structures of hBest1 in the open and partially open states.
A Open state hBest1 (PDB ID 8D1O) and **D** partially open state hBest1 (PDB ID 8D1K) structures visualized with ion permeation pathway in white. The transmembrane neck region of the open state **B** and partially open state **E** structures, with ion permeation pathway colored by hydrophobicity with pale brown corresponding to maximum hydrophobicity and green corresponding to maximum hydrophilicity. Top-down view of **C** the open state neck and **F** partially open state neck. **G** Pore radius profiles of the open, partially open and closed (PDB ID 8D1I) states.

Figure 2: Cl^- binding site analysis.
A Close-up representation of neck residues (I76, F80 and F84) from a single chain highlighted in licorice representation of the open state structure (PDB ID 8D1O). The cryo-EM densities are shown as a mesh representation in purple. A panel is zoomed in on the non-protein ion-like density in proximity to F80 labelled as X739, which corresponds to the water molecule HOH739 in the PDB. **B** The trajectories of water (cyan), sodium (green) and Cl^- (orange) ions in z-coordinates as a function of time within the neck region of the pore. The plot indicates that Cl^- tends to cluster in a region between I76 and F80. The green dashed line represents the location of X739 from the experimental structure. AMOEBA forcefield simulations: Top-down view of the protein fragment in **C** AMOEBA (orange) or F c36m (magenta) aligned to the full protein structure (cyan). The location of X739 is indicated by the green sphere. The top detected binding pose identified with PyLipID shows **D** significant overlap between the AMOEBA Cl^- (orange sphere) and X739, indicating this site likely functions as a Cl^- binding site or **G** the c36m Cl^- (magenta sphere) shares no overlap with X739. **E, H** A rotated view showing the distance of the Cl^- and X739 to the backbone N of F80 in the experimental structure.

Figure 3: Analysis of open state F80 sidechains of AMOEBA simulations.
A Torsion angle χ_2 is defined as the angle CA-CB-CG-CD1. The torsion angle exhibits a discrete two state behavior corresponding to the ring in a flat conformation where $\chi_2 \sim 255°$ or vertical $\chi_2 \sim 285°$. **B** Angle θ is defined as the angle between vectors given by F80 CA and F84 CA of the same chain, and F80 CA with F80 CZ from the aromatic ring. θ gives an indication of the vertical movement of the sidechain in the z-direction. **C** Distance *xy* defines the distance between atom CZ from one chain and the CA atom from F80 in the adjacent chain. This characterizes the sidechain conformation as facing either inward towards the pore axis or outwards as it were in the experimental structure. The graph depicts the moving average over the last 50 frames of the simulation. **D** Snapshots exemplifying the flipping motion of a single F80 sidechain (chain 5). The sidechain simultaneously rotates from a flat aromatic ring position (χ_2), moves vertically in the positive z-direction (θ), and flips inwards (*xy*). Once in the inwards flipped conformation, the aromatic ring may form edgewise anion-π interactions with Cl^-. The flipping motion of the F80 sidechain is reversible. **E** The partial loss of the first hydration shell is compensated by a direct interaction with an inward flipped aromatic ring. Two adjacently flipped aromatic rings can facilitate the loss of multiple water molecules and be compensated through hydrophobic solvation. **F** Coordination number of Cl^- in bulk (blue) compared with at the z-position of F80 (orange) within the pore. Cl^- loses ~1-3 water molecules in its first hydration shell at F80 relative to bulk.

Figure 4: Analysis of the partially open state
Trajectories of water (cyan), sodium (green) and Cl^- (orange) ions in z-coordinates as a function of time within the neck region of the partially open state pore (PDB ID 8D1K) using

A the AMOEBA forcefield or **B** c36m forcefield. The red box in **A** highlights a Cl^- that can occupy locations above F84 in the neck whereas nearly no ions can be seen in **B** with c36m. **C** Bottom-up view of F84 of the partially open state neck. The volume that Cl^- may occupy over the simulation is represented by the orange mesh. **D** Side-view of the neck region. F84 of the neck may accommodate for Cl^-; however, the neck is not permeable to Cl^-. **E** Top-down view of F84. Cl^- can be seen to interact with the aromatic ring through edgewise anion-π interactions. The coordinating atoms within the first solvation shell of the Cl^- (orange sphere) are represented as spheres.

References

1. B. Hille, *Ionic Channels of Excitable Membranes*, 3rd Ed. (Sinauer Associates Inc, 2001).
2. B. Roux, Ion channels and ion selectivity. *Essays Biochem* **61**, 201–209 (2017).
3. F. Ashcroft, *Ion Channels and Disease* (Academic Press, 2000).
4. L. Leisle, *et al.*, Backbone amides are determinants of Cl− selectivity in CLC ion channels. *Nat Commun* **13**, 1–11 (2022).
5. B. C. Garrett, Ions at the Air/Water Interface. *Science* **303**, 1146–1147 (2004).
6. G. Klesse, S. Rao, S. J. Tucker, M. S. P. Sansom, Induced Polarization in Molecular Dynamics Simulations of the 5-HT3 Receptor Channel. *J Am Chem Soc* **142**, 9415–9427 (2020).
7. G. Hantal, J. Kolafa, M. Sega, P. Jedlovszky, Single-Particle Dynamics at the Intrinsic Surface of Aqueous Alkali Halide Solutions. *Journal of Physical Chemistry B* **125**, 665–679 (2021).
8. P. B. Petersen, R. J. Saykally, On the Nature of Ions At the Liquid Water Surface. *Annu Rev Phys Chem* **57**, 333–364 (2006).
9. P. Bajaj, *et al.*, Halide Ion Microhydration: Structure, Energetics, and Spectroscopy of Small Halide-Water Clusters. *Journal of Physical Chemistry A* **123**, 2843–2852 (2019).
10. P. A. Gale, Anion receptor chemistry. *Chemical Communications* **47**, 82–86 (2011).
11. S. Chakravarty, A. R. Ung, B. Moore, J. Shore, M. Alshamrani, A Comprehensive Analysis of Anion-Quadrupole Interactions in Protein Structures. *Biochemistry* **57**, 1852–1867 (2018).
12. M. R. Jackson, *et al.*, A preference for edgewise interactions between aromatic rings and carboxylate anions: The biological relevance of anion-quadrupole interactions. *Journal of Physical Chemistry B* **111**, 8242–8249 (2007).
13. L. M. Breberina, M. K. Milčić, M. R. Nikolić, S. D. Stojanović, Contribution of anion-π interactions to the stability of Sm/LSm proteins. *Journal of Biological Inorganic Chemistry* **20**, 475–485 (2015).
14. S. Jojoa-Cruz, *et al.*, Structural insights into the Venus flytrap mechanosensitive ion channel Flycatcher1. *Nat Commun* **13**, 1–11 (2022).
15. Y. H. Chen, *et al.*, Homologue structure of the SLAC1 anion channel for closing stomata in leaves. *Nature* **467**, 1074–1080 (2010).
16. Z. Deng, *et al.*, Structural mechanism for gating of a eukaryotic mechanosensitive channel of small conductance. *Nat Commun* **11**, 1–9 (2020).
17. J. P. Renaud, *et al.*, Cryo-EM in drug discovery: Achievements, limitations and prospects. *Nat Rev Drug Discov* **17**, 471–492 (2018).
18. E. D'Imprima, W. Kühlbrandt, Current limitations to high-resolution structure determination by single-particle cryoEM. *Q Rev Biophys* **54**, 1–15 (2021).
19. M. Beckers, D. Mann, C. Sachse, Structural interpretation of cryo-EM image reconstructions. *Prog Biophys Mol Biol* **160**, 26–36 (2021).
20. Ł. Nierzwicki, G. Palermo, Molecular Dynamics to Predict Cryo-EM: Capturing Transitions and Short-Lived Conformational States of Biomolecules. *Front Mol Biosci* **8**, 1–6 (2021).
21. P. E. M. Lopes, B. Roux, A. D. MacKerell, Molecular modeling and dynamics studies with explicit inclusion of electronic polarizability: Theory and applications. *Theor Chem Acc* **124**, 11–28 (2009).
22. J. W. Ponder, *et al.*, Current status of the AMOEBA polarizable force field. *Journal of Physical Chemistry B* **114**, 2549–2564 (2010).
23. J. Huang, P. E. M. Lopes, B. Roux, A. D. MacKerell, Recent advances in polarizable force fields for macromolecules: Microsecond simulations of proteins using the

classical drude oscillator model. *Journal of Physical Chemistry Letters* **5**, 3144–3150 (2014).
24. V. Ngo, *et al.*, Polarization Effects in Water-Mediated Selective Cation Transport across a Narrow Transmembrane Channel. *J Chem Theory Comput* **17**, 1726–1741 (2021).
25. H. I. Okur, *et al.*, Beyond the Hofmeister Series: Ion-Specific Effects on Proteins and Their Biological Functions. *Journal of Physical Chemistry B* **121**, 1997–2014 (2017).
26. S. Rao, G. Klesse, P. J. Stansfeld, S. J. Tucker, M. S. P. Sansom, A BEST example of channel structure annotation by molecular simulation. *Channels* **11**, 347–353 (2017).
27. A. P. Owji, A. Kittredge, Y. Zhang, T. Yang, Structure and Function of the Bestrophin family of calcium-activated chloride channels. *Channels* **15**, 604–623 (2021).
28. T. Yang, *et al.*, Structure and selectivity in bestrophin ion channels. *Science* **346**, 355–359 (2014).
29. A. P. Owji, *et al.*, Structures and gating mechanisms of human bestrophin anion channels. *Nat Commun* **13**, 1–11 (2022).
30. A. P. Owji, *et al.*, Structural and functional characterization of the bestrophin-2 anion channel. *Nat Struct Mol Biol* **27**, 382–391 (2020).
31. G. Klesse, S. J. Tucker, M. S. P. Sansom, Electric Field Induced Wetting of a Hydrophobic Gate in a Model Nanopore Based on the 5-HT3Receptor Channel. *ACS Nano* **14**, 10480–10491 (2020).
32. L. X. Phan, *et al.*, Influence of electronic polarization on the binding of anions to a chloride-pumping rhodopsin. *Biophys J* **122**, 1548–1558 (2023).
33. W. G. Hol, P. T. van Duijnen, H. J. Berendsen, The alpha-helix dipole and the properties of proteins. *Nature* **273**, 443–446.
34. V. K. Dickson, L. Pedi, S. B. Long, Structure and insights into the function of a Ca2+-activated Cl- channel. *Nature* **516**, 13–218 (2014).
35. W. Song, *et al.*, PyLipID: A Python Package for Analysis of Protein-Lipid Interactions from Molecular Dynamics Simulations. *J Chem Theory Comput* **18**, 1188–1201 (2022).
36. M. Serna, Hands on methods for high resolution cryo-electron microscopy structures of heterogeneous macromolecular complexes. *Front Mol Biosci* **6**, 1–8 (2019).
37. Z. Zhao, D. M. Rogers, T. L. Beck, Polarization and charge transfer in the hydration of chloride ions. *Journal of Chemical Physics* **132**, 1–10 (2010).
38. M. I. Chaudhari, J. M. Vanegas, L. R. Pratt, A. Muralidharan, S. B. Rempe, Hydration Mimicry by Membrane Ion Channels. *Annu Rev Phys Chem* (2020) https:/doi.org/10.1146/annurev-physchem-012320.
39. D. T. Gomez, L. R. Pratt, D. N. Asthagiri, S. B. Rempe, Hydrated Anions: From Clusters to Bulk Solution with Quasi-Chemical Theory. *Acc Chem Res* **55**, 2201–2212 (2022).
40. A. Dhotel, *et al.*, Molecular motions in functional self-assembled nanostructures. *Int J Mol Sci* **14**, 2303–2333 (2013).
41. X. Kan, H. Liu, Q. Pan, Z. Li, Y. Zhao, Anion-π interactions: From concept to application. *Chinese Chemical Letters* **29**, 261–266 (2018).
42. G. Vaisey, A. N. Miller, S. B. Long, Distinct regions that control ion selectivity and calcium-dependent activation in the bestrophin ion channel. *Proc Natl Acad Sci U S A* **113**, E7399–E7408 (2016).
43. A. N. Miller, G. Vaisey, S. B. Long, Molecular mechanisms of gating in the calcium-activated chloride channel bestrophin. *Elife* **8**, 1–17 (2019).
44. L. X. Phan, C. I. Lynch, J. Crain, M. S. P. Sansom, S. J. Tucker, Influence of effective polarization on ion and water interactions within a biomimetic nanopore. *Biophys J* **121**, 2014–2026 (2022).

45. F. Lin, A. D. M. Jr, Improved Modeling of Cation- π and Anion-Ring Interactions Using the Drude Polarizable Empirical Force Field for Proteins. 439–448 (2020).
46. S. Rao, *et al.*, Water and hydrophobic gates in ion channels and nanopores. *Faraday Discuss* **209**, 231–247 (2018).
47. S. Jo, T. Kim, V. G. Iyer, W. Im, CHARMM-GUI: A web-based graphical user interface for CHARMM. *J Comput Chem* **29**, 1859–1865 (2008).
48. M. J. Abraham, *et al.*, Gromacs: High performance molecular simulations through multi-level parallelism from laptops to supercomputers. *SoftwareX* **1–2**, 19–25 (2015).
49. D. J. Evans, B. L. Holian, The Nose-Hoover thermostat. *J Chem Phys* **83**, 4069–4074 (1985).
50. M. Parrinello, A. Rahman, Polymorphic transitions in single crystals: A new molecular dynamics method. *J Appl Phys* **52**, 7182–7190 (1981).
51. U. Essmann, *et al.*, A smooth particle mesh Ewald method. *J Chem Phys* **103**, 8577–8593 (1995).
52. B. Hess, H. Bekker, H. J. C. Berendsen, J. G. E. M. Fraaije, LINCS: A Linear Constraint Solver for Molecular Simulations. *J Comput Chem* **18**, 1463–1472 (1997).
53. C. Zhang, *et al.*, AMOEBA Polarizable Atomic Multipole Force Field for Nucleic Acids. *J Chem Theory Comput* **14**, 2084–2108 (2018).
54. Y. Shi, *et al.*, Polarizable atomic multipole-based AMOEBA force field for proteins. *J Chem Theory Comput* **9**, 4046–4063 (2013).
55. M. Tuckermar, B. J. Berne, G. J. Martyna, Reversible multiple time scale molecular dynamics. *Journal of Chemical Physics* **97**, 1990–2001 (1992).
56. R. J. Gowers, *et al.*, MDAnalysis: A Python Package for the Rapid Analysis of Molecular Dynamics Simulations in *Proc. of the 15th Python in Science Conference*, (2016), pp. 98–105.
57. N. Michaud-Agrawal, E. J. Denning, T. B. Woolf, O. Beckstein, MDAnalysis: A toolkit for the analysis of molecular dynamics simulations. *J Comput Chem* **32**, 2319–2327 (2011).
58. M. J. Abraham, *et al.*, Gromacs: High performance molecular simulations through multi-level parallelism from laptops to supercomputers. *SoftwareX* **1–2**, 19–25 (2015).
59. G. Klesse, S. Rao, M. S. P. Sansom, S. J. Tucker, CHAP: A Versatile Tool for the Structural and Functional Annotation of Ion Channel Pores. *J Mol Biol* **431**, 3353–3365 (2019).

Figure 1

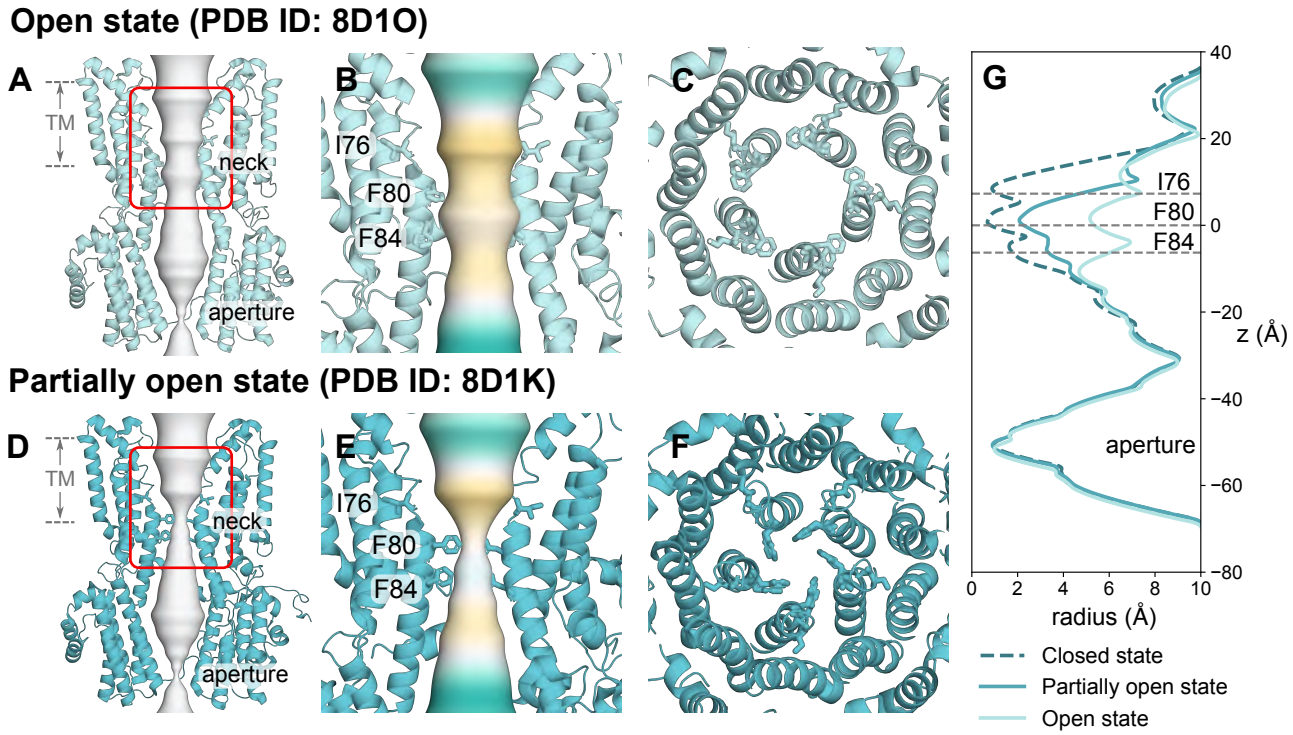

Figure 2

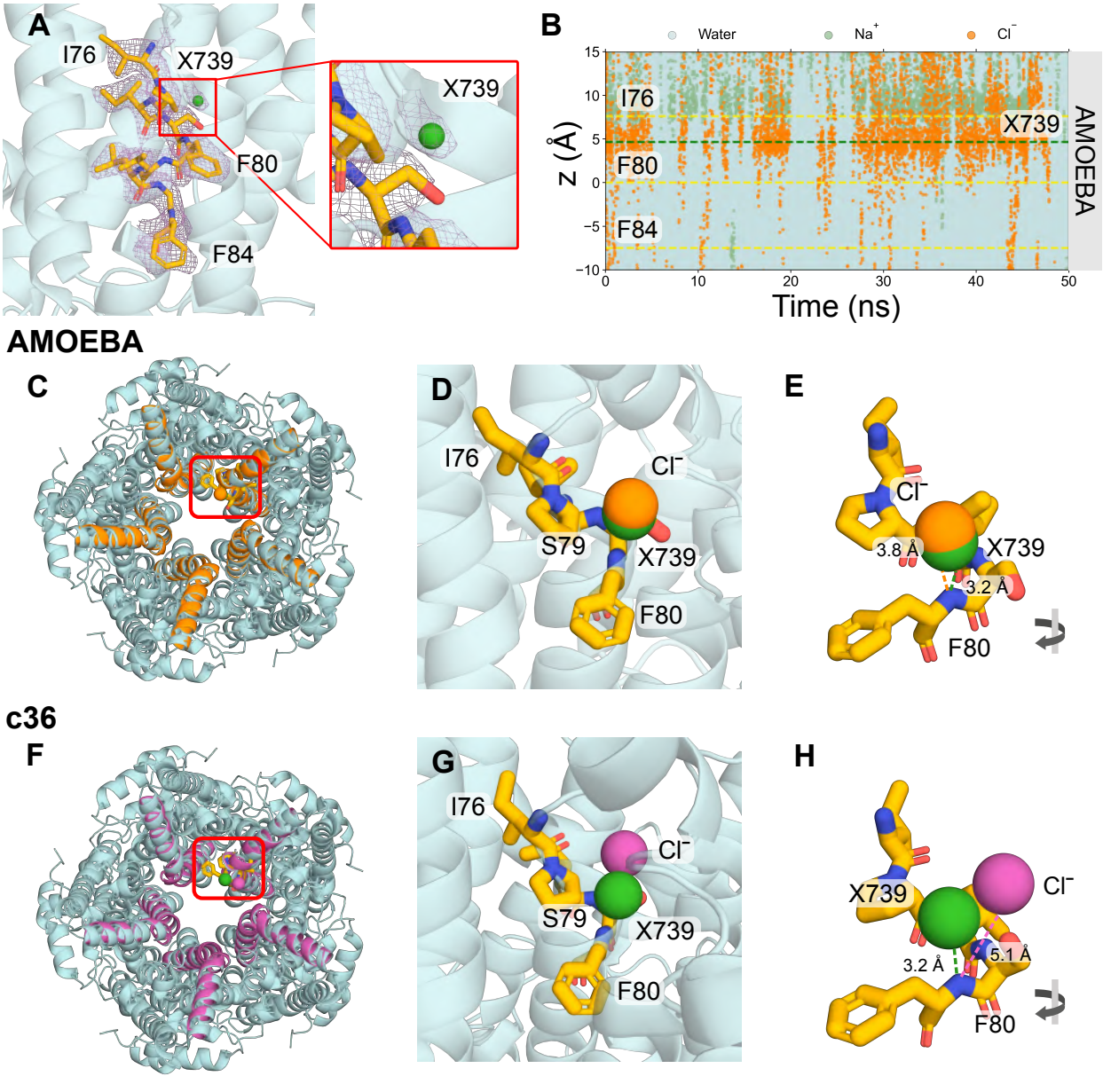

Figure 3

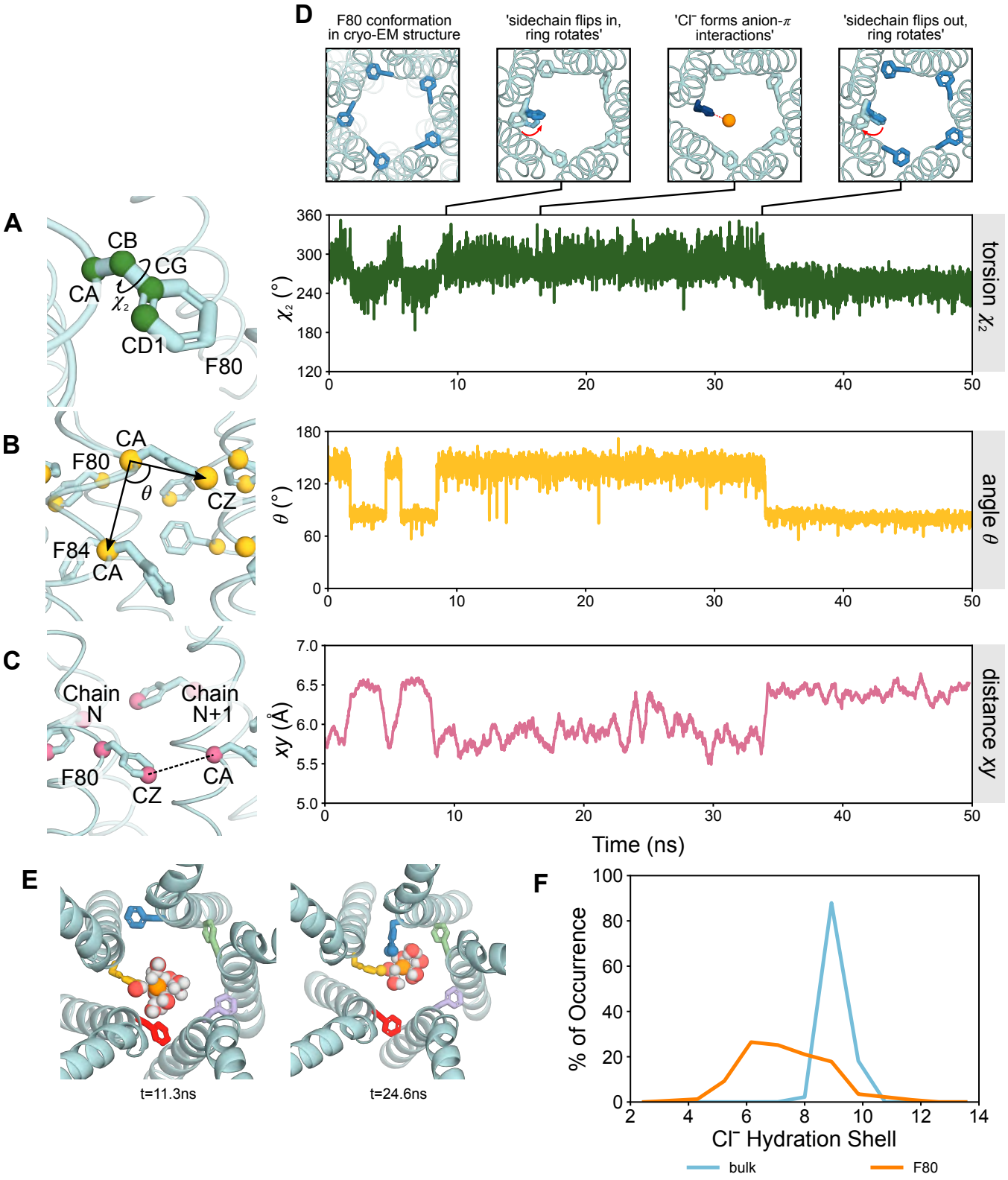

Figure 4

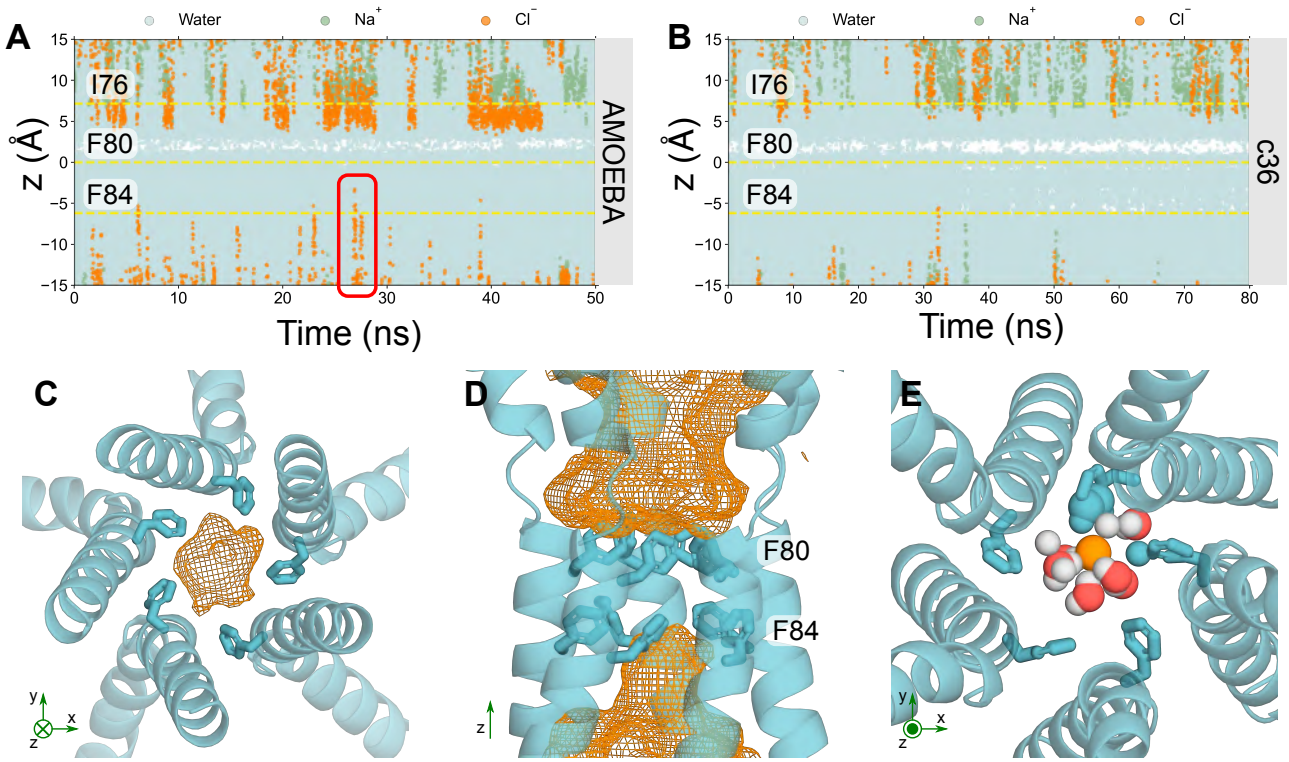

Supplementary Information

Electronic Polarizability Tunes the Function of the Human Bestrophin 1 Chloride Channel

Linda X. Phan, Aaron P. Owji, Tingting Yang, Jason Crain, Mark S.P. Sansom, and Stephen J. Tucker

Supplementary Methodological Details

Full protein embedded simulations

The full protein systems were prepared using a multiscale procedure. The protein is first coarse-grained (CG) and then embedded into a POPC bilayer and solvating with water and ~ 0.5 M NaCl using Martini version 2.2 (1) and GROMACS 2021 package (2). This system is subject to 100 ns of equilibration in CG before being converted to atomistic representation with the CG2AT protocol (3). An equilibration period of 20 ns followed by a production run of 100 ns using the c36m forcefield (4) and mTIP3P water model was performed. The temperature was maintained at 310 K with coupling constant 1.0 ps by the Nosé-Hoover thermostat (5). Pressure was maintained at 1 bar with coupling constant 5.0 ps by the Parrinello-Rahman barostat (6). Short-range electrostatics were treated with the Verlet cutoff scheme at 1.2 nm cutoff and long-range electrostatics were treated with PME(7). C-alpha atoms were placed under harmonic restraints with a force constant of 1000 kJ/mol/nm^2 to prevent the structure from deviating too much from the experimental structure.

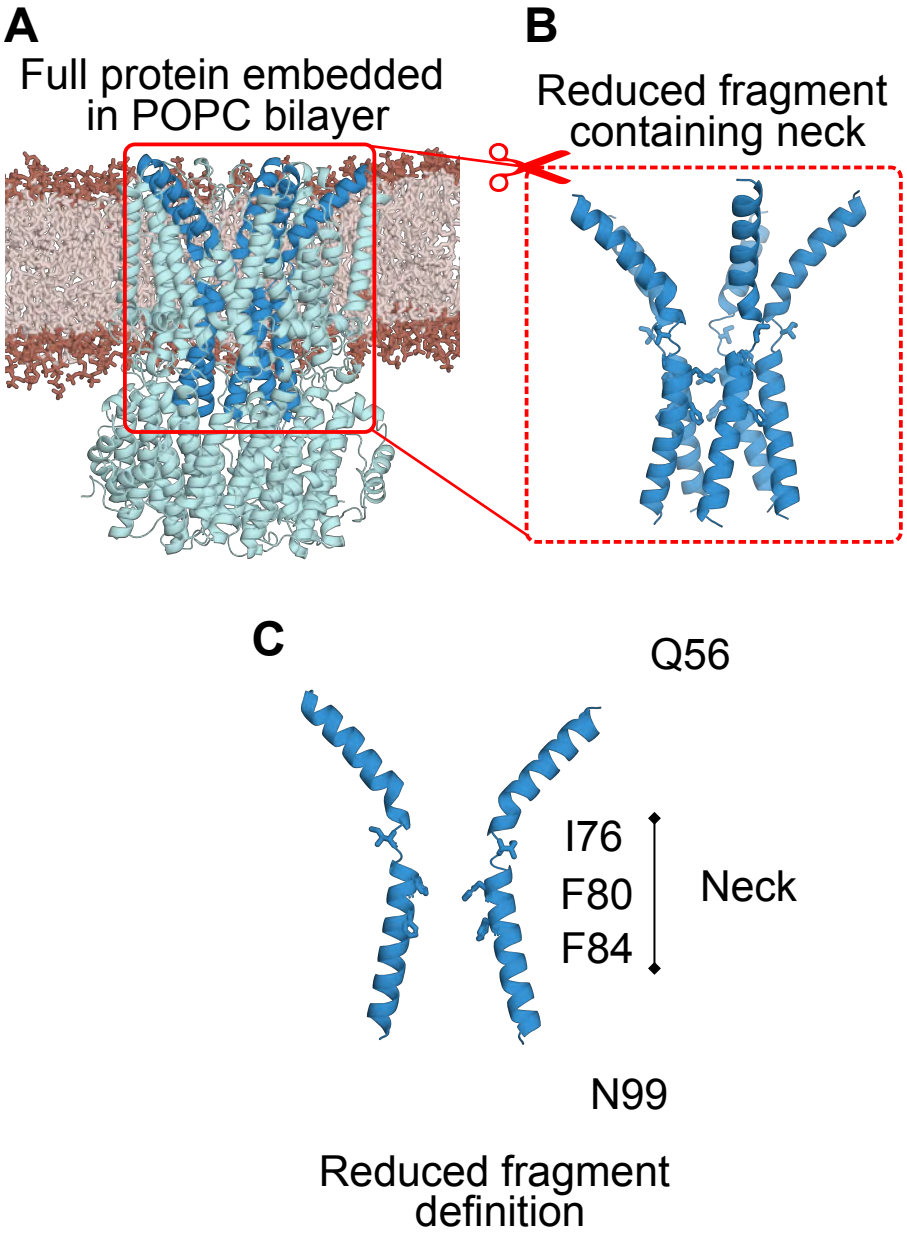

Figure S1: **A** Full protein (cyan) embedded in POPC bilayer (brown). **B** Protein fragment system used in simulations due to the high computational demands of the AMOEBA forcefield. The full protein embedded system in solution contains ~200500 atoms. **C** The protein was truncated at Q56 and N99 such that the remaining fragment system contains the conserved hydrophobic neck region of interest (I76, F80, F84). The reduced protein fragment in solution contains ~57000 atoms. Water and ions are omitted for clarity.

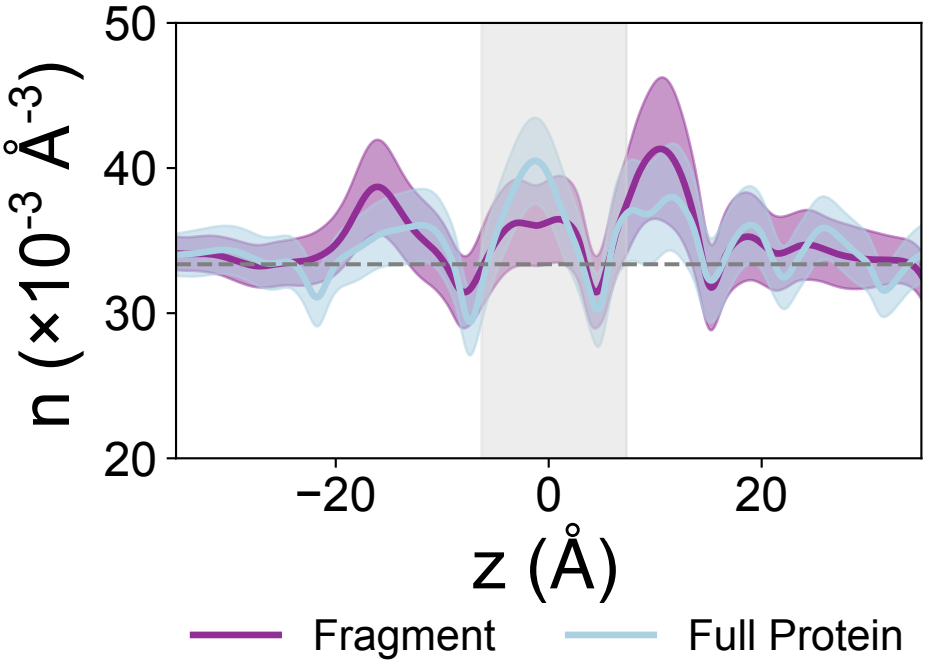

Figure S2: Protein fragment system validation. Time-averaged water density profiles within the pore for the full protein embedded system (light blue) compared with the protein fragment in solution (purple) using c36m. The shaded region represents the neck region, and the dashed grey line corresponds to the density of bulk water (33.37 nm^{-3}). Confidence bands represent the standard deviation over the simulation.

AMOEBA

Binding site 2

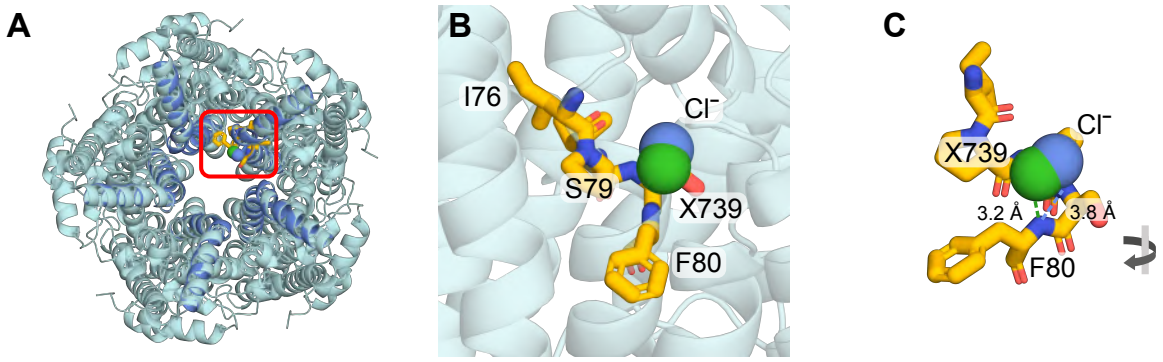

Binding site 3

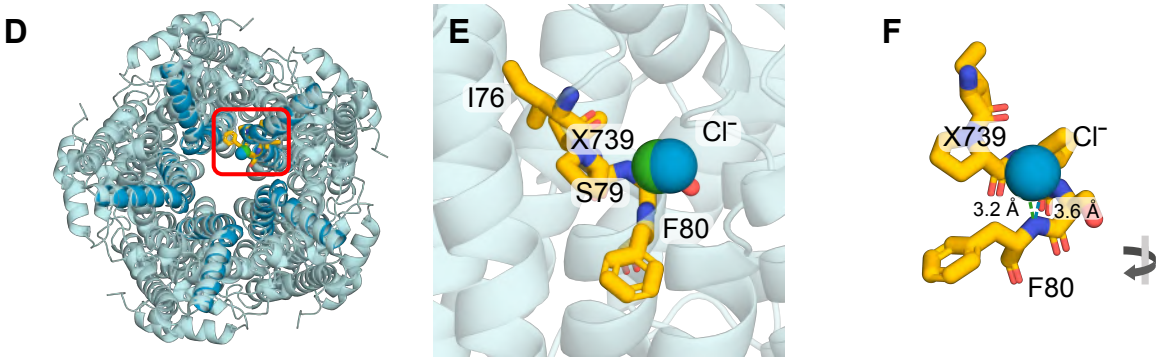

G

Binding Site	Site Residence Time (ns)	k_{off}	Duration (ns)	Occupancy (%)	R-squared	Distance to N of F80 (Å)	Distance to X739 in PDB (Å)
3	0.59	1.7	0.75	14	0.9987	3.8	1.2
12	0.43	2.3	0.63	28	1	3.6	0.7
2	0.34	3.0	0.63	18	0.9999	3.8	0.6

Figure S3: Alternative AMOEBA binding sites of the open state structure (PDB ID 8D1O). **A-C** Binding site 3 and **D-F** show binding site 12. Table **G** gives the binding site statistics where binding site 2 is the site shown in Fig. 2 in the main manuscript.

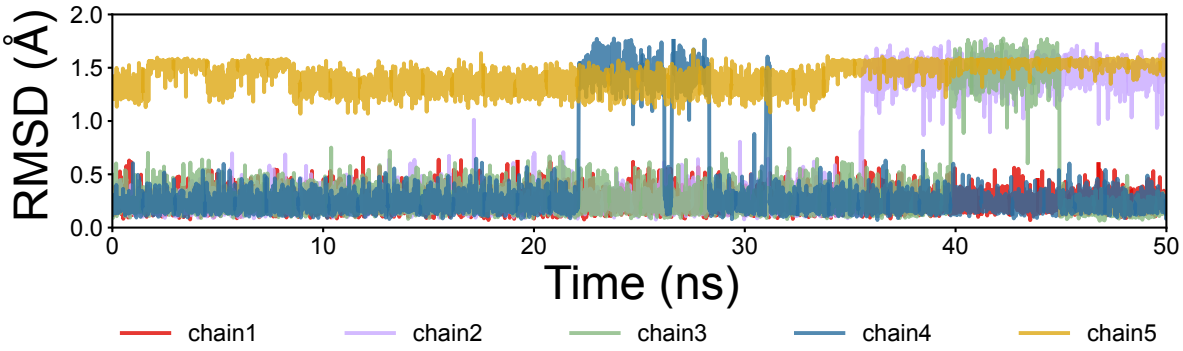

***Figure S4**:* RMSD of F80 sidechain per chain of the open state (PDB ID 8D1O) protein fragment over the AMOEBA simulation.

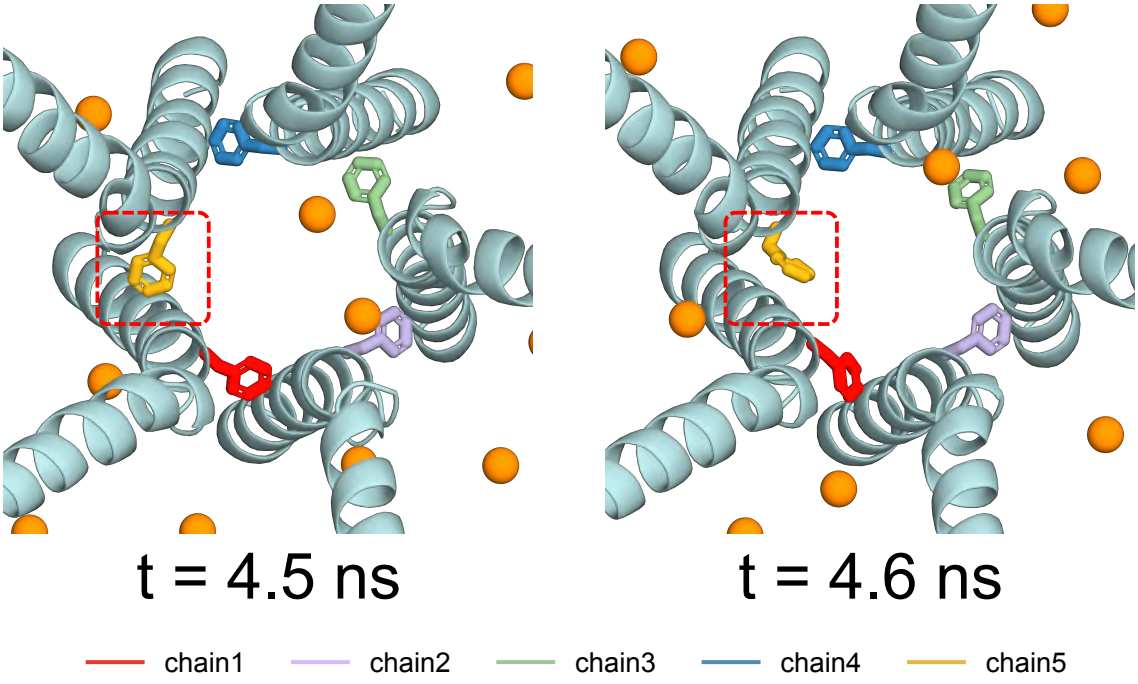

Figure 5: Snapshots demonstrating the spontaneous inwards flipping of an F80 sidechain in the AMOEBA simulation. This motion is not necessarily induced by a passing chloride ion (orange spheres).

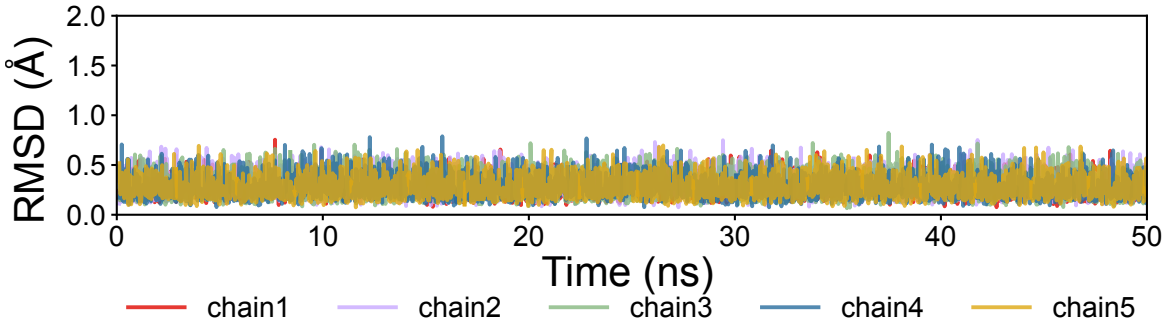

Figure S6: RMSD of F80 sidechains in the partially open state (PDB ID 8D1K). The sidechains remain stable throughout the AMOEBA simulation.

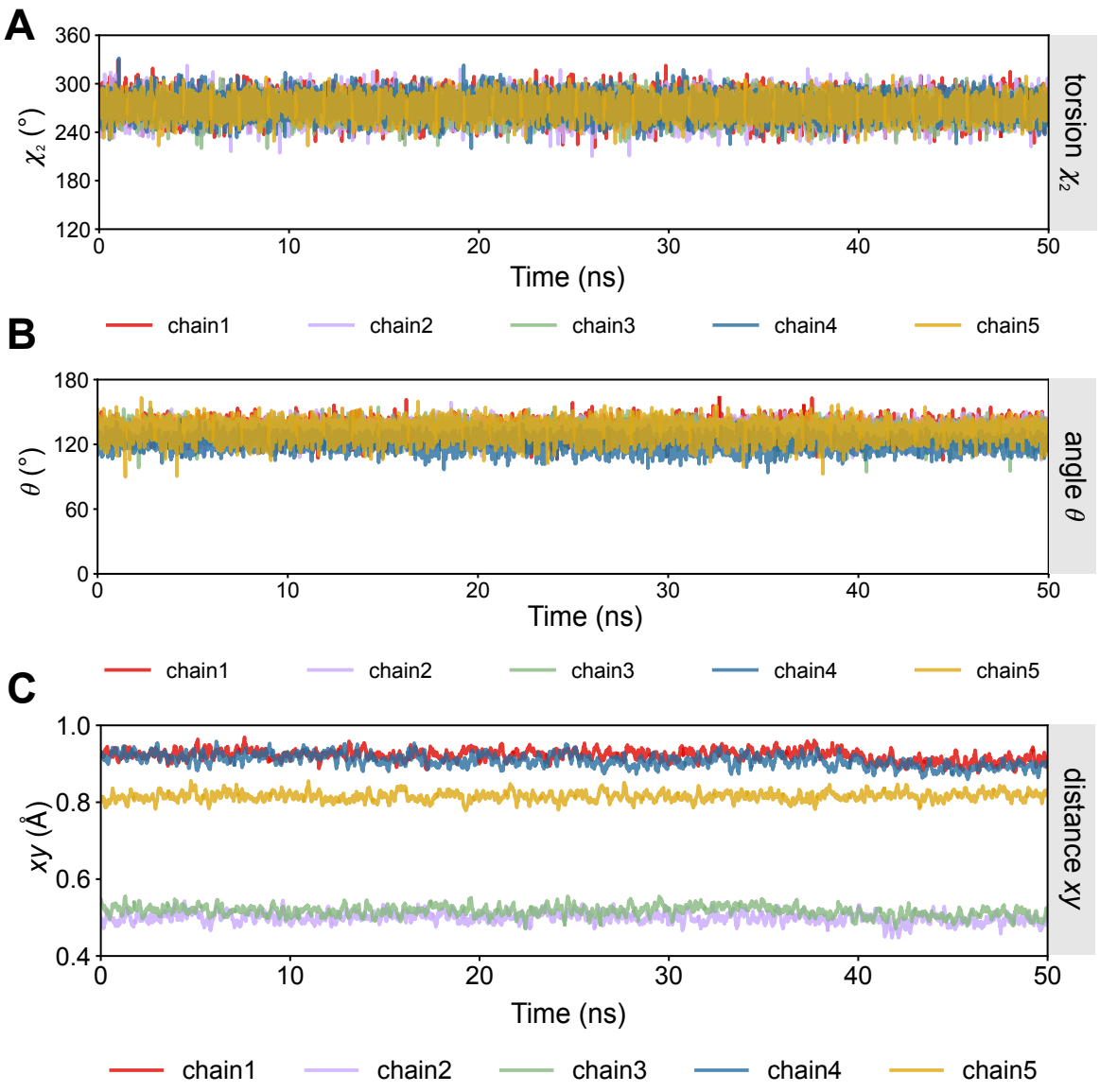

Figure S7: Per chain **A** torsion angle χ_2, **B** angle θ and **C** distance *xy* of F80 in AMOEBA simulation of the partially open state (PDB ID 8D1K). The sidechains remain largely stable in this conformation.

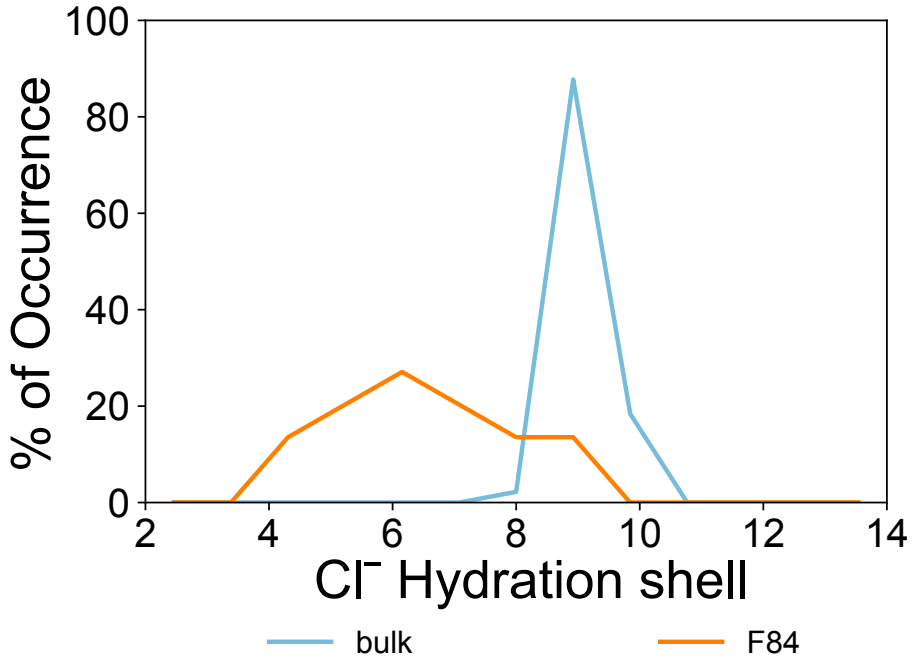

Figure S8: Coordination number of chloride ions in the partially open state structure (PDB ID 8D1K) in bulk (blue) compared with at the z-position corresponding to F84 (orange) within the pore in the AMOEBA simulation. Chloride loses 1-3 water molecules in its first hydration shell at F84 relative to bulk. This is comparable to the dehydration that occurs at F80 in the fully open state (PDB ID 8D1O).

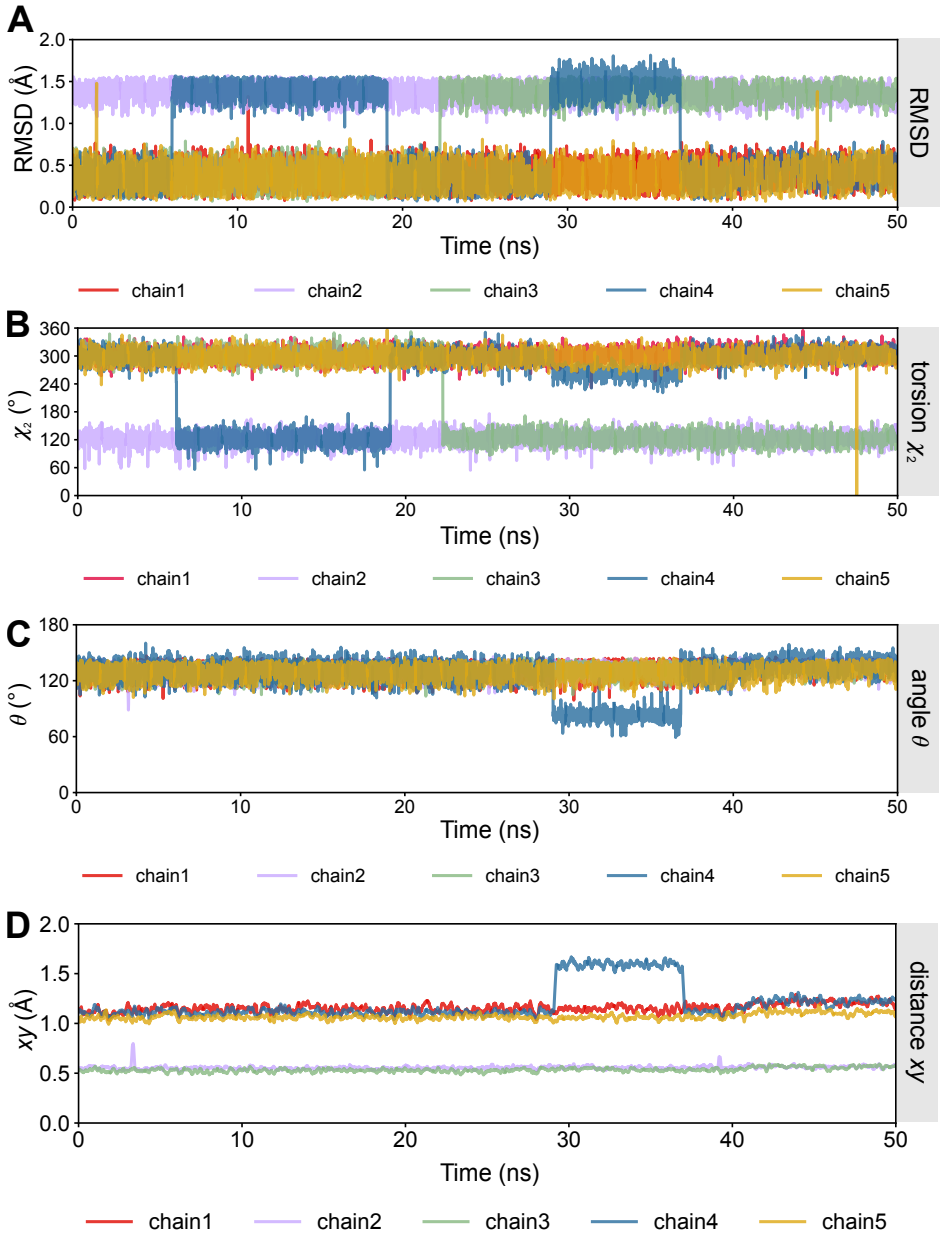

Figure S9: Per chain **A** RMSD, **B** torsion angle χ_2, **C** angle θ and **D** distance *xy* of F84 in the partially open state (PDB ID 8D1K) AMOEBA simulation. The sidechains are largely stable. The two-state behaviour seen in the RMSD and torsion angle correspond to a 180° rotation of the aromatic ring; however, due to the symmetric properties of the aromatic ring, this does not represent an alternative ring conformation. Chain 2 experiences some motion corresponding to an outwards flipping of the sidechain for ~ 7 ns and chain 4 experiences a stochastic downwards flipping motion at ~ 30 – 37 ns.

Supporting information references

1. D. H. De Jong, *et al.*, Improved parameters for the martini coarse-grained protein force field. *J Chem Theory Comput* **9**, 687–697 (2013).
2. M. J. Abraham, *et al.*, Gromacs: High performance molecular simulations through multi-level parallelism from laptops to supercomputers. *SoftwareX* **1–2**, 19–25 (2015).
3. O. N. Vickery, P. J. Stansfeld, CG2AT2: An Enhanced Fragment-Based Approach for Serial Multi-scale Molecular Dynamics Simulations. *J Chem Theory Comput* **17**, 6472–6482 (2021).
4. J. Huang, *et al.*, CHARMM36m: An improved force field for folded and intrinsically disordered proteins. *Nat Methods* **14**, 71–73 (2016).
5. D. J. Evans, B. L. Holian, The Nose-Hoover thermostat. *J Chem Phys* **83**, 4069–4074 (1985).
6. M. Parrinello, A. Rahman, Polymorphic transitions in single crystals: A new molecular dynamics method. *J Appl Phys* **52**, 7182–7190 (1981).
7. U. Essmann, *et al.*, A smooth particle mesh Ewald method. *J Chem Phys* **103**, 8577–8593 (1995).